RSC Advances

PAPER

View Article Online
View Journal | View Issue

Cite this: *RSC Adv.*, 2018, **8**, 25802

Bandgap engineering of a lead-free defect perovskite $Cs_3Bi_2I_9$ through trivalent doping of Ru^{3+}†

Jinyu Gu,[ab] Gangbin Yan,[ab] Yuebin Lian,[ab] Qiaoqiao Mu,[ab] Huidong Jin,[ab] Zaichao Zhang,[c] Zhao Deng *[ab] and Yang Peng *[ab]

Received 24th May 2018
Accepted 9th July 2018

DOI: 10.1039/c8ra04422h

rsc.li/rsc-advances

Inorganic defect halide compounds such as $Cs_3Bi_2I_9$ have been regarded as promising alternatives to overcome the instability and toxicity issues of conventional perovskite solar cells. However, their wide indirect bandgaps and deep defect states severely limit their photoelectronic conversion efficiency when implemented in devices. Trivalent cation substitution has been proposed by previous calculations allowing the engineering of their band structures, but experimental evidences are still lacking. Herein we use the trivalent cation Ru^{3+} to partially replace Bi^{3+} in $Cs_3Bi_2I_9$, and reveal their structural and optoelectronic properties, as well as the environmental stability. The Ru-doped $Cs_3Bi_2I_9$ shows a decreasing bandgap with the increasing doping levels and an overall up-shift of band structure, owing to the dopant-induced defect states and thus enhanced phonon–electron coupling. As a result, upon Ru^{3+} doping, the narrowed bandgap and the upward shift of the band structures might facilitate and broaden their applications in optoelectronic devices.

1 Introduction

Recently perovskite materials have attracted great attention for their promising applications in optoelectronic devices such as solar cells, light emitting diodes, and photodetectors.[1–6] In particular, the photoelectron conversion efficiency (PCE) of hybrid organic–inorganic perovskite solar cells (PSCs) has increased rapidly since 2009,[7] reaching more than 22% up to date.[8] However, the toxicity and instability of these conventional alkylamine-based PSCs have greatly restricted their larger scale production outside laboratories. In this context, photoabsorbers based on inorganic lead-free perovskites have been pursued as potential alternatives, including three major families: $AM^{II}X_3$,[9,10] $A_2M^{I}M^{III}X_6$ [11–13] and $A_3M_2^{III}\square X_9$ [14,15] (A = Cs, Rb; M^{II} = Sn, Ge; M^{I} = Ag, Na, K; M^{III} = Bi, Sb; □ = vacancy sites; X = Cl, Br, I), each representing the halide perovskites, double halide perovskites and defect halide perovskites, respectively. With the choice of different elements for A, M and X, the bandgap of these compounds can be effectively tuned.[16] Further in each of the above perovskite families, the metal M of various chemical states can be further substituted with alloys containing multiple metals with the same total oxidation state (so-called cation transmutation),[17,18] adding an additional degree of freedom to regulate their bandgaps.

In the defect halide perovskite family $A_3M_2^{III}\square X_9$, $Cs_3Bi_2I_9$ has been mostly studied with the consideration of Bi^{3+} having similar electronic structure and ion radius to Pb^{2+}, but much less toxicity.[19–21] At room temperature, $Cs_3Bi_2I_9$ exhibits a distorted and defect-modulated hexagonal perovskite structure, in which a pair of $[BiI_6]^{3-}$ octahedral share faces to form a $[Bi_2I_9]^{3-}$ bioctahedra, and every third layer of the octahedral Bi sites is depleted for charge neutrality, resulting in a zero-dimensional (0D) molecular salt crystal structure (space group $P6_3/mmc$).[22] The 0D structure with separated $[Bi_2I_9]^{3-}$ bioctahedra leads to low carrier mobility and therefore poor charge transport, which might be more beneficial for optical properties, rather than photovoltaic applications.[23–25] For instance, colloidal $Cs_3Bi_2I_9$ nanocrystals have shown unique absorption spectra arising from the 0D crystal structure, with a very high excitonic binding energy of 300 meV.[23] $Cs_3Bi_2I_9$ possesses an average indirect optical bandgap of ~2 eV, with variations reported from different studies.[24] DFT calculations indicated a higher effective mass of charge carriers and prominent deep-level defects for $Cs_3Bi_2I_9$ when compared with their Pb counterparts, and pointed out that defect passivation through external doping or nonequilibrium synthesis might lead to better photovoltaic performance.[25] Solar cells with

[a]Soochow Institute for Energy and Materials Innovations, College of Physics, Optoelectronics and Energy, Collaborative Innovation Center of Suzhou Nano Science and Technology, Soochow University, Suzhou 215006, P. R. China. E-mail: zdeng@suda.edu.cn; ypeng@suda.edu.cn

[b]Key Laboratory of Advanced Carbon Materials and Wearable Energy Technologies of Jiangsu Province, Soochow University, Suzhou 215006, P. R. China

[c]Jiangsu Key Laboratory for the Chemistry of Low-dimensional Materials, School of Chemistry and Chemical Engineering, Huaiyin Normal University, Huai'an 223000, P. R. China

† Electronic supplementary information (ESI) available: SEM images, EDAX data, XPS data, TG curves and ICP data. See DOI: 10.1039/c8ra04422h

$Cs_3Bi_2I_9$ as the photoabsorber has shown a power conversion efficiency over 1% with enhanced chemical stability and additional room for improvement.[27] Hence, in order to further promote the performance of $Cs_3Bi_2I_9$ based optoelectronic devices, bandgap engineering is essential to narrow the optical bandgap, tune the defect chemistry and optimize the electronic structure.[16,28,29] For example, DFT studies by Hong *et al.* inferred that the bandgap of $Cs_3Bi_2I_9$ can be reduced by applying dual trivalent metal cations to form $Cs_3BiM^{III}I_9$,[18] although there has been no experimental evidence in this regard.

Discovered since the 1980s', $Cs_3Ru_2Cl_9$ is another compound of the $A_3M_2^{III}\square X_9$ family that also belongs to the $P6_3/mmc$ space group with bioctahedra $[Ru_2Cl_9]^{3-}$.[30,31] Inspired by this fact, herein we attempt to dope the $Cs_3Bi_2I_9$ with various concentrations of Ru^{3+} through atomic substitution of Bi^{3+} in order to regulate its bandgap and optical properties. As a result, crystals of $Cs_3Bi_{2-x}Ru_xI_9$ with dimensions from several to hundreds of micrometers were obtained by a hydrothermal approach. Through changing the molar ratio of $RuCl_3$ and BiI_3, various doping levels of Ru^{3+} were realized without altering the crystal structure. Measurements using Raman, UV-Vis, Photoluminescence and Ultraviolet Photoelectron Spectroscopy illustrated that even with a small doping amount, the band structure and optical properties of $Cs_3Bi_{2-x}Ru_xI_9$ can change significantly. Consequently, through effective tuning of the bandgap, defect states and electronic structure, Ru-doped $Cs_3Bi_2I_9$ perovskites exhibit a great perspective for future optoelectronic applications.

2 Experimental section

2.1 Materials and preparation

All chemicals were purchased from the Aladdin Company (China) with purity above 99.95% and used without further purification.

$Cs_3Bi_2I_9$. Microcrystals of $Cs_3Bi_2I_9$ were synthesized by the hydrothermal method. In a 50 mL reactor, 1.5 mmol CsI and 1 mmol BiI_3 were dissolved in 20 mL concentrated HI acid. The reactor was then sealed and placed into a thermal oven with the temperature hold at 120 °C. After 6 hours, the temperature was turned down at 10 °C/30 min to the room temperature. Powders of red colour were precipitated from the precursor solution. The solids were then filtered out, washed repeatedly with ethanol and diluted HI, and finally dried under vacuum at 60 °C for overnight.

$Cs_3Bi_{2-x}Ru_xI_9$ (x = 0.02, 0.04, 0.1, 0.2). Microcrystals of $Cs_3Bi_{2-x}Ru_xI_9$ were also synthesized by the hydrothermal method. 1.5 mmol CsI, a mmol BiI_3 and b mmol $RuCl_3$ ($a + b = 2$) were dissolved in 20 mL concentrated HI acid in a 50 mL reactor. The reactor was then sealed and placed into a thermal oven at 120 °C for 6 h. After cooling down, powders of dark red colour were precipitated from the precursor solution. The solids were then filtered out, washed repeatedly with ethanol and diluted HI, and finally dried under vacuum at 60 °C for overnight.

2.2 Characterization

The powder X-ray diffraction (XRD) measurements were conducted using a D8 Advance diffractometer (Bruker Corporation, Germany) operating at 40 kV and 40 mA with Cu Kα radiation (λ = 1.5406 Å), and the scanning rate was fixed at 4° min^{-1}. Scanning electron microscopy (SEM) images and Energy Dispersive X-ray spectroscopy (EDX) were taken by a FEI Scios Microscope (Thermo Fisher, USA). Transmission electron microscope (TEM) images and elemental mapping were taken by the FEI 200 kV G20 Microscope (Thermo Fisher, USA). X-ray photoelectron spectroscopy (XPS) and Ultraviolet Photoelectron Spectroscopy (UPS) were performed on an Escalab 250Xi (Thermo Fisher, USA). For UPS measurements, pristine Au was used to calibrate the Fermi level. Raman spectra were obtained on a Jobin Yvon HR Evolution Spectrometer (Horiba, Japan). Fluorescence Spectroscopy was taken with a FLS980 Fluorescence Spectrometer (Edinburgh instruments, UK). Thermogravimetric analysis (TGA) was conducted with the SII TG/DTA7200 (Japan) at a rate of 20 °C min^{-1} ramping from room temperature to 700 °C inside a crucible. UV-Vis spectroscopy was recorded with PerkinElmer Lambda 750S (USA).

3 Results and discussion

3.1 Crystalline phase and morphology

As reported previously, $Cs_3Bi_2I_9$ crystallizes in the $P6_3/mmc$ space group with a lattice constant of a = 8.335 Å and c = 21.326 Å (Fig. 1a).[16] When a portion of Bi^{3+} sites in $Cs_3Bi_2I_9$ is substituted with Ru^{3+}, the colour of the crystal powder changes from bright to dark red with the increasing doping level (Fig. 1b). The darkened colour is indicative of narrowed bandgap, as more visible light is absorbed by the compound. The PXRD data of $Cs_3Bi_{2-x}Ru_xI_9$ with x = 0, 0.02, 0.04, 0.1 and 0.2 are given in Fig. 1c (also amplified in Fig. S1†), from which one can see that at low doping levels, the XRD patterns exhibit no obvious change from the original $Cs_3Bi_2I_9$ spectrum, matching well the standard profile of JCPDS no. 39-1346. This suggests the lattice structure of $Cs_3Bi_2I_9$ is not observably affected by low levels of Ru^{3+} substitution, likely due to the smaller atomic radius of Ru^{3+} than Bi^{3+} (Fig. 1a). However, at a higher level of substitution (x = 0.2), more broadened brag peaks can be observed at 26°, 28°, 31°and 44°, which could be

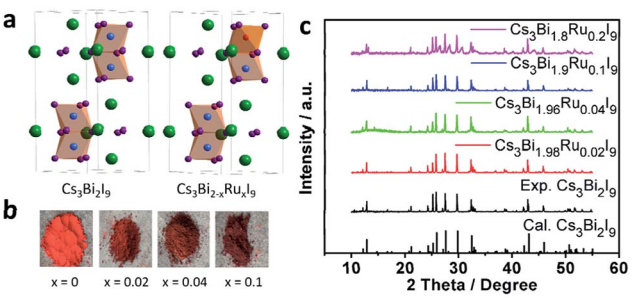

Fig. 1 (a) Crystal structure of $Cs_3Bi_2I_9$ and $Cs_3Bi_{2-x}Ru_xI_9$. (b) Photos of samples synthesized in this work showing darkened colour with increasing Ru^{3+} doping. (c) Powder XRD of $Cs_3Bi_2I_9$ and $Cs_3Bi_{2-x}Ru_xI_9$ with x = 0.02, 0.04, 0.1, 0.2.

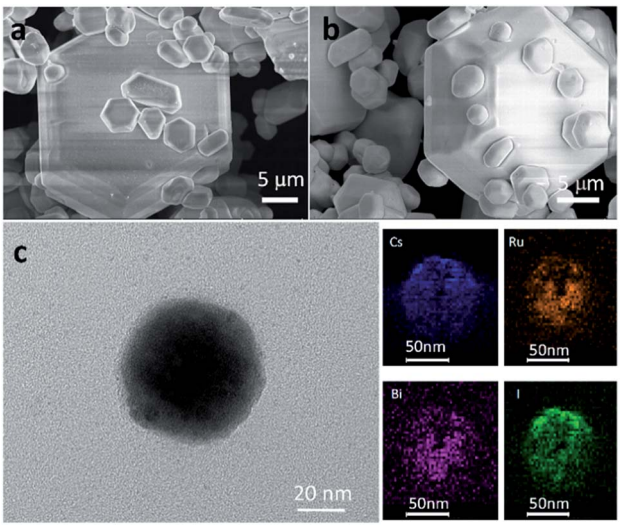

Fig. 2 (a) and (b) SEM images of $Cs_3Bi_2I_9$ and $Cs_3Bi_{1.9}Ru_{0.1}I_9$, respectively. (c) TEM image of $Cs_3Bi_{1.9}Ru_{0.1}I_9$ and the corresponding elemental mapping of Cs, Bi, Ru, and I.

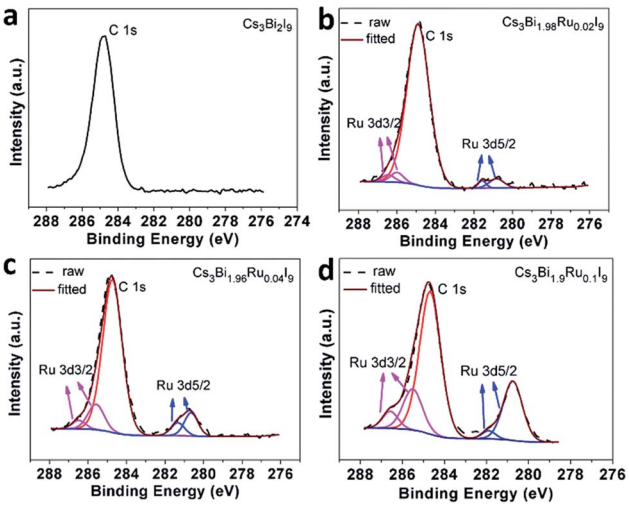

Fig. 3 XPS spectra of Ru^{3+} for $Cs_3Bi_{2-x}Ru_xI_9$ showing the increase of peak intensity with increasing doping levels. (a) $x = 0$; (b) $x = 0.02$; (c) $x = 0.04$; (d) $x = 0.1$.

resulted from possible structural corruption, as evidenced by morphological changes from the scanning electron microscopy (SEM) characterization (Fig. S2†) and that none of these peaks is assignable to any raw materials.

Fig. 2a and b present the characteristic SEM images of the as-prepared $Cs_3Bi_2I_9$ and $Cs_3Bi_{1.9}Ru_{0.1}I_9$ microcrystals, respectively. Particles of various size ranging from a few to hundreds of microns can be found throughout the samples. While small particles exhibit more irregular crystal shapes, those larger ones are typically hexagonal. Simultaneously, energy-dispersive X-ray spectroscopy (EDX) measurements were taken to verify the existence of Ru^{3+} in the doped samples, all showing prominent Ru peaks (Fig. S3†). Fig. 2c presents the TEM image of a small particle of $Cs_3Bi_{1.9}Ru_{0.1}I_9$, with the corresponding elemental mapping clearly showing that atoms of Bi and Ru are homogeneously distributed within the crystal.

XPS analysis of surface atomic chemical states reveals all Cs, Bi, I elements for $Cs_3Bi_2I_9$ and the additional Ru element for $Cs_3Bi_{2-x}Ru_xI_9$ (Fig. 3 and S4†). No obvious shift of chemical states is observable for Cs, Bi, and I elements upon Ru-doping. There is a carbon peak at 284.9 eV in all spectra of tested samples, attributable to atmospheric carbon introduced during the sample preparation and testing process. Neighboring to the C peak, the Ru 3d peaks are composed of two doublets, assignable to Ru $3d_{3/2}$ centered at around 286.0 eV and Ru $3d_{5/2}$ at around 281.0 eV. The XPS analysis not only proves the successful doping of Ru into $Cs_3Bi_2I_9$, but also confirms its trivalent chemical state. In addition, the intensity of the Ru $3d_{5/2}$ doublet increases monotonically with the doping level. To further quantify the actual doping concentration of Ru^{3+} in replacement of Bi^{3+} in different $Cs_3Bi_{2-x}Ru_xI_9$ samples, elemental analysis by Inductively Coupled Plasma-Atomic Emission Spectrometry (ICP-AES) was carried out on the obtained crystals and the results are listed in the Table S1.† For a theoretical doping concentration of 0, 1%, 2% and 5% based on the molar ratio of added $RuCl_3$ to $BiCl_3$, the corresponding ICP-AES reading is 0, 0.9%, 1.9% and 4.3%, respectively. The discrepancy between the theoretical and actual Ru-doping levels could be caused by both incomplete reaction and weighting errors, but overall a good correlation between the two can be seen as long as the doping level isn't too high (>5%). For the purpose of convenience and clarification, we use the theoretical doping level to label all samples throughout this study.

3.2 Electronic and optical properties

Raman spectra were taken to illustrate the evolution of chemical bonding and lattice configuration inside the $Cs_3Bi_{2-x}Ru_xI_9$ crystals with increasing Ru^{3+} doping (Fig. 4). Within the wavenumber range from 50 cm^{-1} to 2000 cm^{-1}, the obtained spectrum for each compound at room temperature reveals similar crystal structure. No peaks were found above 200 cm^{-1}, and all compounds have six major peaks at the same positions without apparent peak shift. The position of these six peaks is in good agreement with what reported for $Cs_3Bi_2I_9$ before,[26,32] where the three peaks at higher wave number (high energy peaks) are

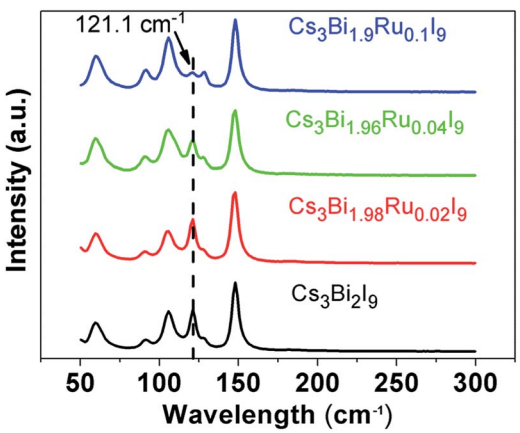

Fig. 4 Raman spectra of the $Cs_3Bi_{2-x}Ru_xI_9$ ($x = 0$, 0.02, 0.04, and 0.1) samples.

resulted from symmetric and asymmetric stretches of the terminal Bi–I bonds in the $[Bi_2I_9]^{3-}$ anion, and the middle two peaks at 105.8 cm^{-1} and 91.6 cm^{-1} are caused by symmetric and asymmetric stretches of the bridging Bi–I bonds, respectively.[33] On the far left side, the low energy peak at 59.4 cm^{-1} represents the bending modes of the Bi–I bonds. A prominent trend observed from the Raman spectra is the gradual disappearance of the antisymmetric peak at 121.1 cm^{-1} with the increasing Ru^{3+} doping. Since both of the atomic mass and radius of Ru is smaller than Bi, one of the asymmetric stretches associated with it is likely to induce less inelastic scattering of the laser light, resulting in the weakened antisymmetric mode. As the peak at 121.1 cm^{-1} represents one of the two terminal Bi–I asymmetric stretches, this indicates the replacement of Bi with Ru has higher impact on the terminal Bi–I stretches than on the bridging B–I stretches, owing to the stronger force constants of the terminal Bi–I bonds as the bridging I atoms share their bonds with two Bi atoms.[32] The doping of Ru^{3+} in replacement of Bi^{3+} further causes local lattice distortions, as indicated by the Raman spectral evolution, and creates new defect states as well as enhanced electron–phonon coupling, both enabling to trap excitons upon irradiated absorption.

As shown in the optical images in Fig. 1b, the color of the compounds turns darker as the doping amount of Ru^{3+} increases. To further quantify the light absorption and optical bandgaps of the $Cs_3Bi_{2-x}Ru_xI_9$ compounds with various Ru^{3+} doping, UV-Vis diffuse reflectance spectra were taken as shown in Fig. 5a. All acquired UV-Vis spectra display similar curves with a stronger absorption observed with the increasing Ru^{3+} amount. For all samples, the absorption starts from around 630 nm with an additional peak observed near 490 nm, corresponding to the $n = 1$ excitonic transition as seen previously.[34] From the UV spectra, the optical bandgap can be estimated according to the equation below:

$$[F(R)h\nu]^n = A(h\nu - E_g) \quad (1)$$

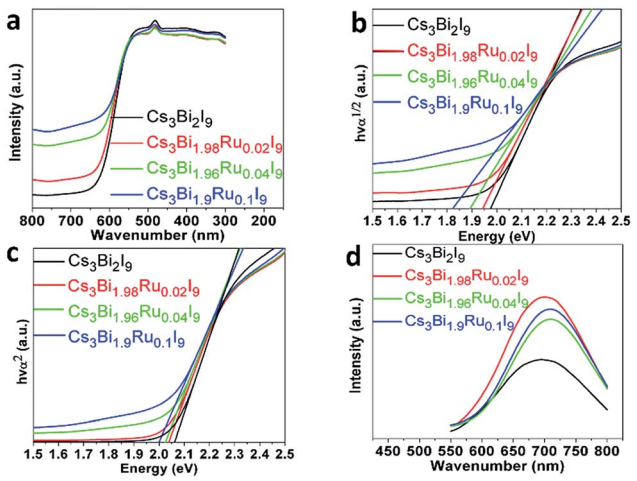

Fig. 5 (a) The UV-Vis spectra of $Cs_3Bi_{2-x}Ru_xI_9$. (b) The direct Tauc plots of $Cs_3Bi_{2-x}Ru_xI_9$. (c) The indirect Tauc plots of $Cs_3Bi_xRu_{2-x}I_9$. (d) The normalized PL spectra of $Cs_3Bi_{2-x}Ru_xI_9$.

where $h\nu$ is the photon energy, A is a proportional constant, E_g is the value of the band gap, $n = 2$ for a direct transition or 1/2 for an indirect transition, and $F(R)$ is the Kubelka–Munk function. By linearly extrapolating $[F(R)h\nu]^n = 0$, indirect optical bandgaps from 1.98 eV to 1.81 eV (Fig. 5b) and direct bandgaps from 2.07 eV to 1.98 eV (Fig. 5c) can be deduced for $Cs_3Bi_{2-x}Ru_xI_9$ with increasing Ru^{3+} doping. The bandgap value of pristine $Cs_3Bi_2I_9$ is in good agreement with previous reports,[34–36] and the shift of bandgaps is consistent with the optical color change observed for these compounds.

To better understand the radiative exciton recombination of the Ru-doped $Cs_3Bi_2I_9$ compounds, photoluminescence (PL) measurements were performed (Fig. 5d). All powder samples exhibit relatively broad PL emissions in the wavelength range of 500–900 nm, with the unsubstituted $Cs_3Bi_2I_9$ showing a similar spectrum to previous literature reports.[12,27] The broad PL emission is well-known characteristic of the defect halide perovskites such as $A_3M_2^{III}\square X_9$ due to the strong electron-phonon coupling and defect-mediated recombination, which is evidenced by the observed high emission wavelength (~700 nm) in contrast to the absorption edge (~600 nm). In addition, the electron-phonon interaction causes local distortion of the lattice, generating so-called polarons to couple with carriers and increase their effective mass, and therefore severely broaden the optical spectra.[26] Both of the lattice defects and polarons enable to trap excitons, intercepting the radiative recombination. With the Ru^{3+} doping, all emission peaks of $Cs_3Bi_{2-x}Ru_xI_9$ display a higher intensity and a slight red-shift towards higher wavelength, which further indicates the emission centers belong to some shallow defect-type states, rather than the intrinsic band-edge states.[12,37] The red-shift of PL emissions (from 696 to 706 nm) with increasing Ru^{3+} doping resonates with the narrowed bandgaps as observed in the UV-Vis studies, and might also indicate the defect states become relatively deeper with the increased doping level. This argument is further supported by the fact that the intensity of PL emissions does not linearly increase with the doping level of Ru^{3+}, with the highest intensity observed for $Cs_3Bi_{1.98}Ru_{0.02}I_9$, and then decreased thereafter. Similar phenomena of PL decreasing with increasing dopant has also been seen for In-alloyed $Cs_2AgBiBr_6$ (ref. 38) and Mn-doped $Cs_2AgInCl_6$ (ref. 39) samples.

To examine the effect of Ru-doping on modifying the band structure of $Cs_3Bi_{2-x}Ru_xI_9$, we employed Ultraviolet Photoelectron Spectroscopy (UPS) to measure the position of the valence band maximum (VBM) with respect to the vacuum energy for $Cs_3Bi_2I_9$ and $Cs_3Bi_{1.9}Ru_{0.1}I_9$. Previous protocol developed by Lehner *et al.* was followed to capture and analyze the data and Au was used to calibrate the Fermi level.[19] As shown in Fig. 6, the onset of the UPS spectrum starts from 1.70 eV for $Cs_3Bi_2I_9$ and 1.10 eV for $Cs_3Bi_{1.9}Ru_{0.1}I_9$, with the corresponding cut-off binding energy being 17.02 and 16.82 eV, respectively. Therefore, by calculation the work function of $Cs_3Bi_2I_9$ and $Cs_3Bi_{1.9}Ru_{0.1}I_9$ are 4.20 and 4.40 eV, and their corresponding VBMs are −5.90 and −5.50 eV, respectively. Further based on the optical bandgaps measured from the previously acquired UV-Vis spectra (1.98 eV for $Cs_3Bi_2I_9$ and 1.80 eV for $Cs_3Bi_{1.9}Ru_{0.1}I_9$), we were able to deduce the conduction band minimum (CBM)

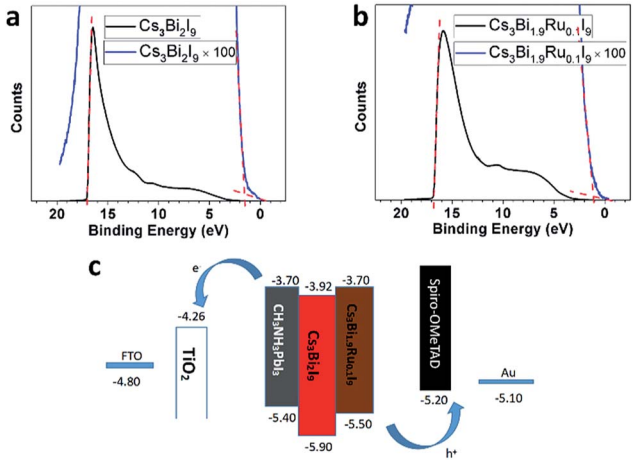

Fig. 6 UPS spectra of (a) $Cs_3Bi_2I_9$ and (b) $Cs_3Bi_{1.9}Ru_{0.1}I_9$. (c) Band structure of $Cs_3Bi_{1.9}Ru_{0.1}I_9$ and $Cs_3Bi_2I_9$ in reference to $MAPbI_3$, TiO_2 and PEDOT:PSS.

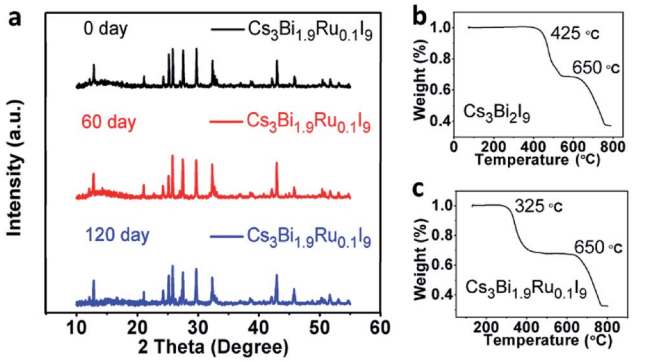

Fig. 7 (a) PXRD spectrum of $Cs_3Bi_{1.9}Ru_{0.1}I_9$ after 60 days and 120 days. (b) and (c)TGA spectra of $Cs_3Bi_2I_9$ and $Cs_3Bi_{1.9}Ru_{0.1}I_9$, respectively.

for $Cs_3Bi_2I_9$ and $Cs_3Bi_{1.9}Ru_{0.1}I_9$, being −3.92 and −3.70 eV respectively. The band positions of $Cs_3Bi_2I_9$ are within the upper and lower bounds of previously reported range (−3.40 to −4.20 eV for CBM, −5.60 to −6.30 eV for VBM).[19] What's more, by comparing Fig. 6a with Fig. 6b, the counts of photoelectrons within the valence band are higher on $Cs_3Bi_{1.9}Ru_{0.1}I_9$, indicative of a higher photoactivity, which is consistent with previous UV and PL results. Fig. 6c shows the column diagram for comparing the band positions of $Cs_3Bi_2I_9$ and $Cs_3Bi_{1.9}Ru_{0.1}I_9$, with the classic perovskite photoabsorber ($MAPbI_3$) and two commonly used hole-transportation (PEDOT:PSS) and electron-transportation (TiO_2) materials as references. Upon doping with ~5% Ru, the valance band position of $Cs_3Bi_{1.9}Ru_{0.1}I_9$ shifts up about 0.40 eV (*vs.* $Cs_3Bi_2I_9$) with a narrowed bandgap of 1.80 eV, and the CBM is close to that of $MAPbI_3$. As a result, both the narrowed bandgap and the upshift of the overall band structure might facilitate their wider optoelectronic applications.

3.3 Environmental and thermal stability

Stability is a key factor when evaluating perovskite materials for potential optoelectronic applications. It was reported that $Cs_3Bi_2I_9$ is more stable than Pb-based perovskites upon exposure to the ambient atmosphere in both light and moisture conditions. To further investigate the stability of Ru-doped $Cs_3Bi_2I_9$, we selected the $Cs_3Bi_{1.9}Ru_{0.1}I_9$ as an example to examine its environmental stability. XRD spectra were acquired after 60 and 120 days of full exposure to the room light and moisture (~60% RH) of lab environments. As shown in Fig. 7a, no obvious change is observable among these spectra, demonstrating excellent environmental stability of the Ru-doped $Cs_3Bi_2I_9$ compounds. Furthermore, we checked the thermal stability of the $Cs_3Bi_{1.9}Ru_{0.1}I_9$ compound under extreme conditions using the thermogravimetric analysis (TGA). A two-step weight loss was seen for both doped and un-doped $Cs_3Bi_2I_9$, with the first weight loss around 30%, likely due to the partial sublimation of one molecule of BiI_3 (bp ≈ 500 °C) from the parent compound.[26] For the pristine $Cs_3Bi_2I_9$, the first decomposition starts from 450 °C, whereas for $Cs_3Bi_{1.9}Ru_{0.1}I_9$ this temperature is lowered to 325 °C. A linear decrease of the first decomposition temperature was seen with the increasing Ru-doping (Fig. S5†). This provides extra evidence for the substitution of Ru^{3+} into the $[Bi_2I_9]^{3-}$ bioctahedra, deteriorating its thermal stability. For all compounds, the second decomposition starts from about 650 °C, coincident with the melting point of CsI (mp ≈ 650 °C) and evaporation of the rest BiI_3. Based on the TG curves, the decomposition products of $Cs_3Bi_{1.9}Ru_{0.1}I_9$ from the two weight-loss stages were further examined by XRD (Fig. S6†), showing the remained product after heating at 600 °C contains both CsI and BiI_3, whereas that after 800 °C contains CsI and elemental Cs. It is worth to note that although the thermal stability of $Cs_3Bi_{2-x}Ru_xI_9$ deteriorates with increasing Ru-doping, they can still tolerate high temperature up to 300 °C, sufficient for most real-world applications.

4 Conclusions

In summary, although $Cs_3Bi_2I_9$ has been viewed as a potential candidate for the photoabsorber of lead-free perovskite solar cells, its relatively high bandgap and deep intrinsic defect states are still the limiting factors for achieving high photoelectric conversion efficiency. In the current study, we have successfully doped Ru^{3+} into $Cs_3Bi_2I_9$ up to 4.3% using a hydrothermal method, and obtained homogeneously dispersed crystals without damaging its crystalline structure. Optical measurements using Raman, UV-Vis and photoluminescent spectroscopy illustrated that even with a small doping amount, the optoelectronic properties of $Cs_3Bi_{2-x}Ru_xI_9$ changes significantly, including narrowed optical bandgap, induced shallow defect states, and more radiative recombination centers. UPS measurements revealed that doping of Ru^{3+} upshifts the overall band structure of $Cs_3Bi_2I_9$ with a higher work function. Stability tests further confirmed the good environmental and thermal stability of $Cs_3Bi_{2-x}Ru_xI_9$. All these results indicate that doping of Ru^{3+} into $Cs_3Bi_2I_9$ allows engineering the band structure by regulating its defect states as well as electronic structure. Consequently, this study shed new light on regulating the optoelectronic properties of the defect halide perovskite family through cation substitution.

Conflicts of interest

There are no conflicts to declare.

Acknowledgements

This work was supported by the 1000 Young Talents Program of China, Natural Science Foundation of China (No. 21701118), Natural Science Foundation of Jiangsu Province (No. K20161209 and No. BK20160323) and the Key Technology Initiative of Suzhou Municipal Science and Technology Bureau (SYG201748). We also extend our sincere appreciation to the support by Suzhou Key Laboratory for Advanced Carbon Materials and Wearable Energy Technologies, Suzhou 215006, China.

Notes and references

1 M. M. Lee, J. Teuscher, T. Miyasaka, T. N. Murakami and H. J. Snaith, *Science*, 2012, **338**, 643–647.
2 N. J. Jeon, J. H. Noh, W. S. Yang, Y. C. Kim, S. Ryu, J. Seo and S. I. Seok, *Nature*, 2015, **517**, 476–480.
3 Z.-K. Tan, R. S. Moghaddam, M. L. Lai, P. Docampo, P. Higler, F. Deschler, M. Price, A. Sadhanala, L. M. Pazos, D. Credgington, F. Hanusch, T. Bein, H. J. Snaith and R. H. Friendan, *Nat. Nanotechnol.*, 2014, **9**, 687–692.
4 L. T. Dou, Y. Yang, J. B. You, Z. R. Hong, W. H. Chang, G. Li and Y. Yang, *Nat. Commun.*, 2014, **5**, 5404–5409.
5 M. Leng, Z. Chen, Y. Yang, Z. Li, K. Zeng, K. Li, G. Niu, Y. He, Q. Zhou and J. Tang, *Angew. Chem., Int. Ed.*, 2016, **55**(48), 15012–15016.
6 J. Y. Gu, P. W. Qi and Y. Peng, *Acta Phys.-Chim. Sin.*, 2017, **33**(7), 1379–1389.
7 A. Kojima, K. Teshima, Y. Shirai and T. Miyasaka, *J. Am. Chem. Soc.*, 2009, **131**, 6050–6053.
8 W. S. Yang, X. Huang, J. H. Noh, Z. Zhao, N. J. Jeon, L. Cao, Y. Chen, Y. C. Kim, E. Zhu and S. Ryu, *Science*, 2015, **348**(6240), 1234–1237.
9 I. Chung, J. H. Song, J. Im, J. Androulakis, C. D. Malliakas, H. Li, A. J. Freeman, J. T. Kenney and M. G. Kanatzidis, *J. Am. Chem. Soc.*, 2012, **134**, 8579–8587.
10 N. Wang, Y. Zhou, M.-G. Ju, H. F. Garces, T. Ding, S. Pang, X. C. Zeng, N. P. Padture and X. W. Sun, *Adv. Energy Mater.*, 2016, **6**, 1601130–1601139.
11 A. H. Slavney, T. Hu, A. M. Lindenberg and H. I. Karunadasa, *J. Am. Chem. Soc.*, 2016, **138**, 2138–2141.
12 J. Zhou, Z. Xia, M. S. Molokeev, X. Zhang, D. Peng and Q. Liu, *J. Mater. Chem. A*, 2017, **5**, 15031–15037.
13 E. T. McClure, M. R. Ball, W. Windl and P. M. Woodward, *Chem. Mater.*, 2016, **28**, 1348–1354.
14 B. Saparov, F. Hong, J.-P. Sun, H.-S. Duan, W. Meng, S. Cameron, I. G. Hill, Y. Yan and D. B. Mitzi, *Chem. Mater.*, 2015, **27**, 5622–5632.
15 F. Wei, F. Brivio, Y. Wu, S. Sun, P. D. Bristowe and A. K. Cheetham, *J. Mater. Chem. C*, 2018, **6**, 3573–3577.
16 A. Swarnkar, V. K. Ravi and A. Nag, *ACS Energy Lett.*, 2017, **2**(5), 1089–1098.
17 G. Volonakis, M. R. Filip, A. A. Haghighirad, N. Sakai, B. Wenger, H. J. Snaith and F. Giustino, *J. Phys. Chem. Lett.*, 2016, **7**, 1254–1259.
18 K.-H. Hong, J. Kim, L. Debbichi, H. Kim and S. H. Im, *J. Phys. Chem. C*, 2016, **121**, 969–974.
19 A. J. Lehner, D. H. Fabini, H. A. Evans, C.-A. Hébert, S. R. Smock, J. Hu, H. Wang, J. W. Zwanziger, M. L. Chabinyc and R. Seshadri, *Chem. Mater.*, 2015, **27**, 7137–7148.
20 R. E. Brandt, V. Stevanović, D. S. Ginley and T. Buonassisi, *MRS Commun.*, 2015, **5**, 265–275.
21 M. Lyu, J. H. Yun, M. Cai, Y. Jiao, P. V. Bernhardt, M. Zhang, Q. Wang, A. Du, H. Wang, G. Liu and L. Wang, *Nano Res.*, 2016, **9**(3), 692–702.
22 Y. N. Ivanov, A. A. Sukhovskii, V. V. Lisin and I. P. Aleksandrova, *Inorg. Mater.*, 2001, **37**, 623–627.
23 J. Pal, A. Bhunia, S. Chakraborty, S. Manna, S. Das, A. Dewan, S. Datta and A. Nag, *J. Phys. Chem. C*, 2018, **22**, 10643–10649.
24 J. Pal, S. Manna, A. Mondal, S. Das, K. V. Adarsh and A. Nag, *Angew. Chem., Int. Ed.*, 2017, **56**(45), 14187.
25 B. Ghosh, S. Chakraborty, H. Wei, C. Guet, S. Li, S. Mhaisalkar and N. Mathews, *J. Phys. Chem. C*, 2017, **121**, 17062–17067.
26 K. M. McCall, C. C. Stoumpos, S. S. Kostina, M. G. Kanatzidis and B. W. Wessels, *Chem. Mater.*, 2017, **29**, 4129–4145.
27 B. W. Park, B. Philippe, X. Zhang, H. Rensmo, G. Boschloo and E. M. Johansson, *Adv. Mater.*, 2015, **27**, 6806–6813.
28 R. D. Nelson, K. Santra, Y. Wang, A. Hadi, J. W. Petrich and M. G. Panthani, *Chem. Commun.*, 2018, **54**, 3640–3643.
29 Y. Hu, S. Zhang, X. Miao, L. Su, F. Bai, T. Qiu, J. Liu and G. Yuan, *Adv. Mater. Interfaces*, 2017, **4**, 1700131.
30 D. J. Lockwood, R. W. G. Syme and B. Briat, *J. Phys. C: Solid State Phys.*, 1985, **18**, 1721–1727.
31 B. J. Kennedy, G. A. Heath and T. J. Khoo, *Inorg. Chim. Acta*, 1991, **190**, 265–269.
32 J. Laane and P. W. Jagodzinski, *Inorg. Chem.*, 1980, **19**, 44–49.
33 F. V. Motsnyi, M. V. Vuychik, O. M. Smolanka and E. Y. Peresh, *Funct. Mater.*, 2005, **12**, 491–496.
34 V. F. Machulin, F. V. Motsnyi, O. M. Smolanka, G. S. Svechnikov and E. Y. Peresh, *Low Temp. Phys.*, 2004, **30**, 964–967.
35 A. Nilă, M. Baibarac, A. Matea, R. Mitran and I. Baltog, *Phys. Status Solidi B*, 2017, **254**, 1552805–1552812.
36 E. Y. Peresh, V. I. Sidei, O. V. Zubaka and I. P. Stercho, *Inorg. Mater.*, 2011, **47**, 208–212.
37 G. Volonakis, A. A. Haghighirad, R. L. Milot, W. H. Sio, M. R. Filip, B. Wenger, M. B. Johnston, L. M. Herz, H. J. Snaith and F. Giustino, *J. Phys. Chem. Lett.*, 2017, **8**, 772–778.
38 K.-Z. Du, w. w. Meng, x. m. Wang, y. f. Yan and D. B. Mitzi, *Angew. Chem., Int. Ed.*, 2017, **56**, 8158–8162.
39 N. K. Nandha and A. Nag, *Chem. Commun.*, 2018, **54**, 5205–5208.